

LCAMV: High-Accuracy 3D Reconstruction of Color-Varying Objects Using LCA Correction and Minimum-Variance Fusion in Structured Light

Wonbeen Oh, and Jae-Sang Hyun, *Member, IEEE*

Abstract—Accurate 3D reconstruction of colored objects with structured light (SL) is hindered by lateral chromatic aberration (LCA) in optical components and uneven noise characteristics across RGB channels. This paper introduces lateral chromatic aberration correction and minimum-variance fusion (LCAMV), a robust 3D reconstruction method that operates with a single projector-camera pair without additional hardware or acquisition constraints. LCAMV analytically models and pixel-wise compensates LCA in both the projector and camera, then adaptively fuses multi-channel phase data using a Poisson-Gaussian noise model and minimum-variance estimation. Unlike existing methods that require extra hardware or multiple exposures, LCAMV enables fast acquisition. Experiments on planar and non-planar colored surfaces show that LCAMV outperforms grayscale conversion and conventional channel-weighting, reducing depth error by up to 43.6%. These results establish LCAMV as an effective solution for high-precision 3D reconstruction of nonuniformly colored objects.

Index Terms—Structured light, 3D reconstruction, lateral chromatic aberration, non-uniform color object scanning

I. INTRODUCTION

3D reconstruction using structured light (SL) has been extensively researched for the past 20 years. Its high precision has enabled applications in manufacturing [1], medical imaging [2], and robotics [3]. Recent advances in graphics processing units (GPUs) have expanded the use of 3D geometry to emerging fields such as virtual reality [4] and teleoperation [5]. The rise of computer vision algorithms incorporating artificial intelligence has also unlocked new applications of 3D geometry data, such as spatial AI [6], [7] and robotic AI [8]. As these applications increasingly require capturing real-world objects with both precise geometry and accurate color information, the ability to extract reliable 3D geometry together with true RGB data has become critical. However, achieving such accuracy is particularly difficult for objects with nonuniform surface colors, as color-dependent responses often degrade reconstruction quality.

The first challenge is **lateral chromatic aberration (LCA)**. Because the refractive index of optical lenses varies with wavelength, rays of different colors are refracted by different amounts, affecting both the projector and camera. In a typical

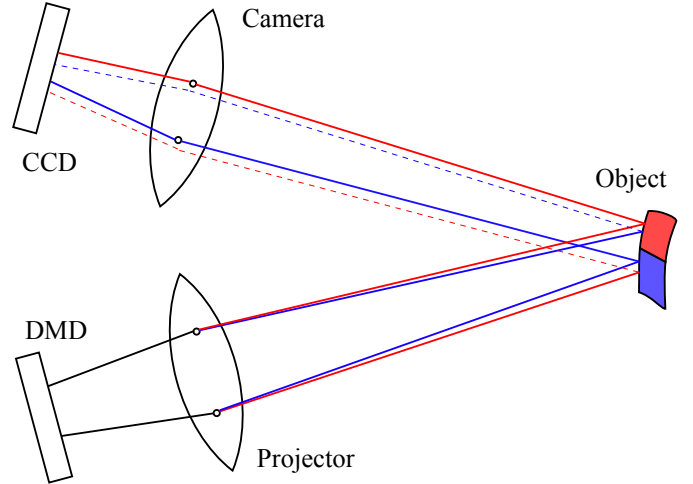


Fig. 1. LCA on scanning a colored object in DFP system.

DMD-based projector, white light is sequentially generated by rapidly displaying red, green, and blue channels. Each color channel follows a slightly different optical path because of LCA in the projector lens, resulting in their projections being spatially shifted on the object surface; similarly, the camera lens introduces additional LCA when capturing these channels. Prior studies [9]–[12] on LCA in digital fringe projection have primarily addressed systems using composite color-fringe patterns, where LCA directly degrades phase-shifting accuracy. However, we emphasize that the LCA is also a critical source of error when scanning nonuniformly colored objects using nominally white fringe patterns. For example, consider scanning a surface containing distinct red and blue regions. In the captured fringe images, the red and blue regions are predominantly illuminated by the projector’s respective red and blue channels, which undergo different refractions due to LCA, as illustrated in Fig. 1.

Beyond LCA, another fundamental difficulty arises from **the unequal sensitivity across the RGB channels**. For a given pixel with channel-wise RGB intensity values, each channel exhibits different sensitivity, depending on the object’s local color. For example, when scanning a red object, the captured image contains the most signal in the red channel, less in the green channel, and predominantly noise in the blue channel. Taking mean intensity across RGB or using predefined weights for RGB to grayscale, such as those Y’UV

Corresponding author: Jae-Sang Hyun

Wonbeen Oh and Jae-Sang Hyun are with the Department of Mechanical Engineering, Yonsei University, Seoul 03722, South Korea. (e-mail: hyun.jaesang@yonsei.ac.kr)

color model [13], is not optimal solution for achieving high reconstruction precision.

A. Related Works

Various approaches have been proposed to simultaneously acquire 3D geometry and texture of colored objects using digital fringe projection. Zhang [14] employed a beam splitter to allow a color camera and a monochrome camera to capture the same scene simultaneously; the monochrome images were used to reconstruct the 3D geometry while the color images provided the RGB texture. In subsequent work, Zhang [15] utilized a single RGB camera by performing phase unwrapping directly on the raw Bayer image and applying bilinear interpolation to obtain the RGB texture. Although this approach reduced the quality of the reconstructed 3D geometry, it enabled simultaneous acquisition of geometry and RGB texture using a single camera. Other studies [16], [17] improved 3D geometry quality by utilizing infrared light, which does not interfere with visible illumination. However, these methods require additional hardware—such as beam splitters, IR light sources, or extra cameras—to achieve accurate simultaneous RGB-D reconstruction. Few studies have rigorously investigated why using RGB images for 3D reconstruction often leads to reduced accuracy. Recently, Wang [18] applied high dynamic range (HDR) imaging with exposure-time adjustment during RGB light projection to mitigate varying signal-to-noise ratios (SNR) caused by nonuniform surface reflectance. However, this method requires multiple captures with varying exposure times and color projections. Yuan [19] proposed robust scanning of colored objects using a specialized 3-PSA code. This method focuses on robustly determining the fringe order for phase unwrapping when scanning colored objects with fewer patterns, rather than minimizing error and improving 3D geometry quality within phase-shifting algorithms. Although both approaches demonstrated robust performance when scanning colored objects, they did not account for LCA effects from either the camera or the projector.

B. Contribution

We propose a novel method, LCAMV (lateral chromatic aberration correction and minimum-variance channel fusion), which robustly reconstructs 3D geometry of nonuniformly colored objects using a single RGB camera and a projector pair, requiring no additional hardware. Furthermore, the method is fully software-based and requires **no additional image captures**, making it potentially applicable to high-speed 3D reconstruction. Our method consists of two stages: 1) Channel-wise LCA correction: Correcting the projector and camera's LCA to align information from the RGB channel properly. 2) Minimum variance channel fusion: Merge aligned RGB information adaptively to maximize the 3D geometry's precision. To the best of our knowledge, this is the first work to explicitly address the LCA in DFP when using nominally white fringe patterns on colored objects.

In this paper, we first analyze the theoretical impact of projector-induced LCA and channel-dependent RGB noise captured by the camera in Section II. We then present our

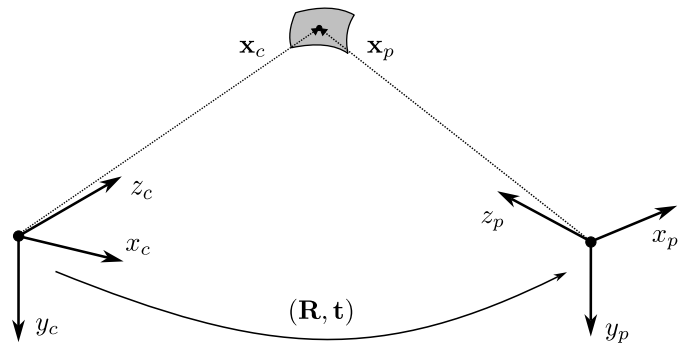


Fig. 2. Structured light system setup

method, which addresses both issues using optical modeling and statistical theory, in Section III. Finally, we validate the proposed approach through real-world experiments in Section IV.

II. PRINCIPLES

3D geometry of an object can be captured with a camera–projector pair in typical DFP. Similar to 3D reconstruction using a stereo-vision system [20], we can consider the projector as an inverse pinhole camera model and conduct *triangulation* as shown in (1). In detail, the geometric relation between the camera and the projector image plane can be represented by the following equation:

$$\mathbf{x}_p = \mathbf{R}\mathbf{x}_c + \mathbf{t} \quad (1a)$$

$$\mathbf{x}_c = s_c \mathbf{K}_c^{-1} \mathbf{u}_c \quad (1b)$$

$$\mathbf{x}_p = s_p \mathbf{K}_p^{-1} \mathbf{u}_p \quad (1c)$$

where $\mathbf{x}_c, \mathbf{x}_p \in \mathbb{R}^3$ are 3D vectors of a point in the camera and projector coordinate systems, and $\mathbf{u}_c, \mathbf{u}_p \in \mathbb{R}^3$ are in pixel coordinates. Note that pixel vectors \mathbf{u} are in homogeneous coordinates: $\mathbf{u}_c = [u_c, v_c, 1]^T$. s_c, s_p are scalar values representing the depth from the camera and projector. $\mathbf{K}_c, \mathbf{K}_p \in \mathbb{R}^{3 \times 3}$ are three-by-three intrinsic matrices which map camera and projector coordinates to pixel coordinates, $\mathbf{R} \in SO(3)$ denotes the rotational matrix, which maps projector to camera coordinates, and $\mathbf{t} \in \mathbb{R}^3$ denotes the translation vector from projector to camera coordinates, as shown in Fig. 2.

Note that $\mathbf{K}_c, \mathbf{K}_p, \mathbf{R}, \mathbf{t}$ are predefined by camera and projector calibration. Given a certain camera pixel (u_c, v_c) , there are four unknowns u_p, v_p, s_p, s_c with three equations. Thus, we can calculate for depth from camera s_c and projector s_p if the projector pixel coordinate is given. In this paper, we will consider the acquisition of the projector's horizontal pixel u_p for 3D geometry reconstruction. Assuming u_p is known, s_c and s_p can be calculated by using the first and third rows of the following equations:

$$s_p \mathbf{u}_p = s_c \mathbf{K}_p \mathbf{R} \mathbf{K}_c^{-1} \mathbf{u}_c + \mathbf{K}_p \mathbf{t} \quad (2)$$

which can be derived from (1). Furthermore, we can solve for the projector's vertical pixel v_p using epipolar constraints:

$$\mathbf{u}_p^T \mathbf{F} \mathbf{u}_c = 0 \quad (3)$$

where $\mathbf{F} = \mathbf{K}_p^{-T}[\mathbf{t}]_{\times} \mathbf{R} \mathbf{K}_c^{-1}$ is a fundamental matrix which can be calculated with calibrated components, and $[\cdot]_{\times}$ is a cross product matrix. v_p will be further used for the LCA correction algorithm in Section III-A. Borrowing the concept of the *phase shifting* from interferometry [21], u_p can be acquired. The projector pixel u_p is scaled to phase ϕ by the following equation:

$$\phi = (2\pi/\lambda) \cdot u_p, \quad \phi \in [0, 2L\pi] \quad (4)$$

where λ is the arbitrarily chosen wavelength of fringe patterns in pixels, and L is the number of phase periods. Note that the $L \cdot \lambda > W_p$ condition should be met, where W_p is the projector pixel width, to fully cover the projector's pixel domain. By capturing the scene upon projection of phase-modulated fringe patterns, we can find corresponding ϕ in the camera image. For the typical three-step phase shifting algorithm [21], the intensity of three captured images in the camera has the following relation:

$$I_1[u_c, v_c] = I_A + I_B \cos\left(\phi - \frac{2}{3}\pi\right) \quad (5a)$$

$$I_2[u_c, v_c] = I_A + I_B \cos(\phi) \quad (5b)$$

$$I_3[u_c, v_c] = I_A + I_B \cos\left(\phi + \frac{2}{3}\pi\right) \quad (5c)$$

where I_1, I_2, I_3 are the captured intensities at the (u_c, v_c) pixel, I_A is the average intensity, and I_B is the modulated intensity by fringe patterns. Note that we can solve for I_A, I_B , and reconstruct the texture of the image upon uniform light projection by adding I_A and I_B [15]. By the three-step phase-shifting algorithm, the wrapped phase ϕ_w can be acquired as follows:

$$\phi_w[u_c, v_c] = \tan^{-1}\left(\frac{\sqrt{3}(I_1 - I_3)}{2I_2 - I_1 - I_3}\right) \quad (6)$$

Note that the wrapped phase ranges $\phi_w \in [-\pi, +\pi)$, thus *phase unwrapping* is required to fully reconstruct original ϕ . Phase unwrapping can be done by acquiring fringe order $l \in \{0, \dots, L-1\}$ using binary gray-code decoding [22] or other phase unwrapping algorithms [23], [24]. Then, the original phase can be reconstructed as follows:

$$\phi = \phi_w + 2\pi l + \pi \quad (7)$$

Given reconstructed ϕ , we can linearly scale into u_p , then solve for (2) to get 3D geometry. Note that multiple number of steps can also be used, by generalized N-step phase shifting algorithm solving least squares [25], [26].

A. Lateral Chromatic Aberration in Camera and Projector

Chromatic aberration (CA) appears in optical systems capturing multiple wavelengths of light. A lens made of glass has a different refractive index with respect to wavelength, which makes light of different colors be projected onto different locations. If this difference is observed parallel to the optical axis, it is called axial chromatic aberration (ACA), and if orthogonal to the optical axis, lateral chromatic aberration (LCA). ACA alters the effective focal length, leading to

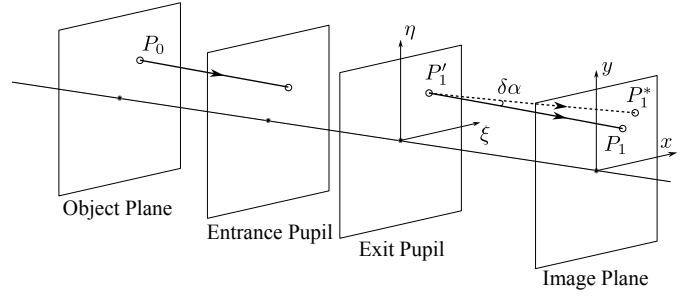


Fig. 3. Aberration in camera system

different blur levels across wavelengths, while LCA shifts the actual projection location on the image plane. Since difference in projection location leads to triangulation error, LCA becomes more problematic when it comes to accurate 3D reconstruction.

Chromatic aberration can be modeled using the *wavefront aberration function* [27], which models the wave aberration Ψ between ideal and real-world optics. In detail, wave aberration can be viewed as a wavefront error, which is an optical path length difference between an ideal spherical wavefront and an actual wavefront. Given wave aberration Ψ , ray aberration $\delta\alpha$, and the resulting lateral aberration at the image plane $\Delta = P_1 - P_1^*$, they can be expressed as follows:

$$\delta\alpha_x = \frac{\partial\Psi}{\partial\xi}, \quad \delta\alpha_y = \frac{\partial\Psi}{\partial\eta} \quad (8a)$$

$$\Delta_x = -\frac{D}{n\gamma}\delta\alpha_x, \quad \Delta_y = -\frac{D}{n\gamma}\delta\alpha_y \quad (8b)$$

where (x, y) are image coordinates and (ξ, η) are pupil coordinates, D is a distance between the exit pupil and the image plane, n is a refractive index of the medium, and γ is a scaling coefficient from (ξ, η) to (x, y) , as shown in Fig. 3.

Under the rotational symmetric assumption, aberration can be approximated using the fourth-order expansion of Ψ , from *Seidel eikonal perturbation* [27]. Considering only the distortion term of the wave aberration function leads to:

$$\Psi(x, y; \xi, \eta) = c(x^2 + y^2)(x\xi + y\eta) \quad (9)$$

where c is a coefficient. Then, we can consider decentering effects in the image plane using perturbations: $x \rightarrow x + \epsilon_x$, $y \rightarrow y + \epsilon_y$. Neglecting ϵ^2 terms, (9) leads to:

$$\Psi(\cdot) = cr^2\kappa^2 + c\xi(\epsilon_x(3x^2 + y^2) + 2\epsilon_y xy) + c\eta(2\epsilon_x xy + \epsilon_y(3y^2 + x^2)) \quad (10)$$

where $r^2 = x^2 + y^2$ and $\kappa^2 = x\xi + y\eta$. Then, we can plug Ψ into (8) to find out the lateral aberration at the image plane. For considering chromatic aberration, the contribution of different refractive indices with respect to wavelengths can be done by adding an extra linear term [28]. Then, the equation for the LCA model leads to:

$$\begin{aligned} \Delta_x^g(\mathbf{x}_f, \mathbf{c}_g) &= c_1 x_f + c_2 x_f r_f^2 + c_3(3x_f^2 + y_f^2) + 2c_4 x_f y_f \\ \Delta_y^g(\mathbf{x}_f, \mathbf{c}_g) &= c_1 y_f + c_2 y_f r_f^2 + 2c_3 x_f y_f + c_4(3y_f^2 + x_f^2) \end{aligned} \quad (11)$$

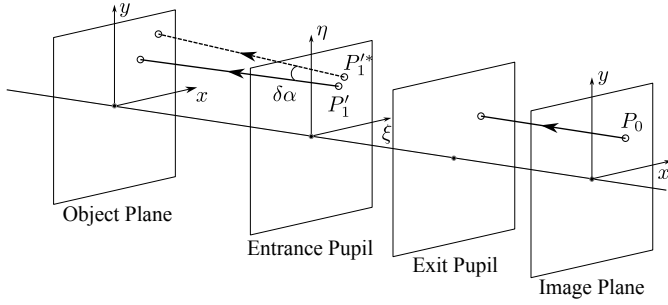


Fig. 4. Aberration in projector system

where $\mathbf{x}_f = [x_f, y_f]$ is an image coordinate vector of the reference wavelength f , and $\mathbf{c}_g = [c_1, c_2, c_3, c_4]$ is a coefficient vector of the specific wavelength g , which has to be corrected. Note that the optical system, including multiple rotational-symmetric components, can be modeled as linear combinations of the same equation [27]; thus, multiple components introduce no additional parameters.

Unlike camera systems where the distance between the image sensor and exit pupil is constrained, the distance between the projector's entrance pupil and the object is not constrained and is comparatively large. Therefore, error induced by the projector's LCA is much larger than the camera's LCA [10], [12]. Inspired by prior works modeling aberration in camera [28] and projector [12], we will model the projector's LCA, treating a projector as an inverse camera model. In the projector system, we have to consider both ray aberration $\delta\alpha$ and lateral aberration $\Delta_E = P'_1 - P_1^*$ at the entrance pupil for optical systems with multiple components, as shown in Fig. 4.

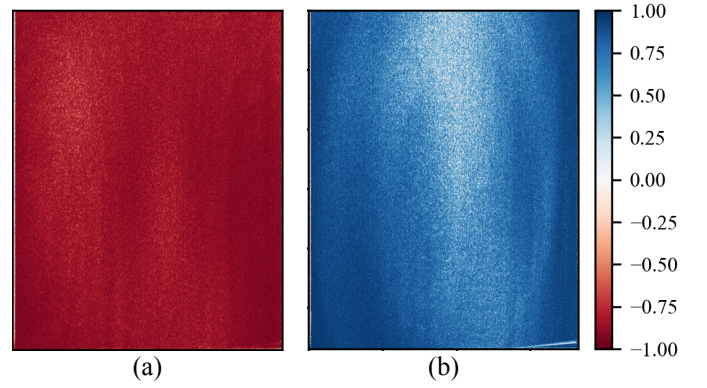
In the camera system it was possible to treat LCA using a depth-independent model since distances between every plane are uniform across all pixels. However, in the projector system, the distance to the object depth z is arbitrary. Therefore, the resulting lateral aberration $\Delta_O = P_1 - P_1^*$ at the object will be a function of z , which can be modeled by a linear model consisting of two parameters α and β as follows.

$$\Delta_O = \alpha \cdot z + \beta \quad (12)$$

where the first-order term is equal to the ray aberration $\alpha = \delta\alpha$, and the constant term represents the distance between the intersections of the two lines, $\overline{P_1^*P_1^*}$ and $\overline{P_1P_1}$, with the image plane at $z = 0$. Note that z is a depth from the projector, which is contradictory in that we need ground truth depth z to compensate for the Δ_O . We use *plug-in error estimation* [29], approximating the depth-dependent Δ_O using the corrupted observation z' under small error assumption. The error between the ground truth $\Delta_O(z)$ and approximated $\Delta_O(z')$ can be expressed as follows:

$$\Delta_O(z) - \Delta_O(z') = \alpha(z - z') \quad (13)$$

Since the depth difference induced by the LCA effect is very small ($z \approx z'$) and the ray aberration coefficient is also small $\alpha \ll 1$, the lateral aberration can be approximated using the initial depth estimate z' . Since we do not have access to


 Fig. 5. Pixel-wise Pearson correlation map of Δ_O and z from channel (a) red (b) blue

the ground-truth depth z , and for notational simplicity, we will use z to denote the estimated depth z' from this point.

Unfortunately, off-the-shelf projectors, which can project arbitrary RGB images, have complicated optical components such as dichroic prisms and mirrors [30]; thus, its LCA is not guaranteed to be modeled using (11) under the rotational-symmetric assumption. To solve this, we used the Look-Up-Table (LUT) approach by actually finding out data points of Δ_O and z for every projector pixel by scanning the white plate.

Fig. 5 is a projector pixel-wise Pearson correlation coefficient [31] map $\rho[u_p, v_p]$ between observed lateral aberration Δ_O and depth z by scanning the white plate. A total of $N = 18$ samples were used from depths ranging in approximately [180, 340] millimeters. It can be found that except for the center-top region of the blue channel where the LCA effect is comparatively low, Δ_O and z are highly linearly correlated with the opposite sign, which shows the validity of our model.

B. Noise Analysis of Intensity and Phase

Due to the nonuniform color setup, some color channels will contain information while others are relatively noisy, depending on the object's surface reflectance. For the noise analysis, we will assume the noise of RGB channels as a *Poisson-Gaussian* model [32], [33] as follows:

$$I[u_c, v_c] = \mu_I[u_c, v_c] + n[u_c, v_c] \quad (14a)$$

$$n \sim \mathcal{N}(0, \sigma_n^2(I)) \quad (14b)$$

$$\sigma_n^2(I) = k_0 + k_1 \cdot I \quad (14c)$$

where μ_I is an ideal ground truth intensity, I is an observed noise-corrupted intensity, and n is an approximated gaussian noise, with variance of σ_n^2 at the (u_c, v_c) pixel. The variance of the noise is approximated with a linear model, where coefficient k_0 models a signal-independent read noise and k_1 models a signal-dependent shot noise of the captured image. Note that due to different optical properties of the Bayer color filter and different gain across RGB channels, noise parameters k_0 and k_1 would be different with respect to RGB channels.

Recall that 3D geometry reconstruction is done by triangulation using a delegate projector pixel, ϕ . To find the contribution

of the intensity and its noise to the acquired phase ϕ , we should model the uncertainty of phase σ_{ϕ}^2 , deriving from phase shifting algorithms. According to [34], under the constant Gaussian noise assumption, the variance of the wrapped phase error using the generalized N-step phase shifting algorithm can be expressed as:

$$\sigma_{\phi_w}^2 \approx \frac{2\sigma^2}{NI_B^2} \quad (15)$$

where σ^2 is the variance of intensity noise. In our Poisson-Gaussian model, the variance of the noise is a function of intensity as shown in (14). From (15), we replace the constant variance σ^2 using the mean noise level $\bar{\sigma}_n^2$ across intensities I_i . Since $\sigma_{n_i}^2$ is linearly proportional to intensity, mean noise level is simply the noise of the mean intensity I_A . Then, (15) under the Poisson-Gaussian model leads to:

$$\sigma_{\phi_w}^2 \approx \frac{2(k_0 + k_1 I_A)}{NI_B^2} \quad (16)$$

where I_A is the mean intensity and I_B is the modulation intensity. For the exemplary three-step phase-shifting algorithm, I_A, I_B can be calculated as follows:

$$I_A = (I_1 + I_2 + I_3)/3 \quad (17a)$$

$$I_B = \sqrt{3(I_1 - I_3)^2 + (2I_2 - I_1 - I_3)^2}/3 \quad (17b)$$

We can consider the numerator term as the mean noise $\bar{\sigma}_n^2 = k_0 + k_1 I_A$, and the denominator term is the square of the modulated signal I_B due to fringe image projections. Then, the uncertainty of phase $\sigma_{\phi_w}^2$ is inversely proportional to SNR. In this paper, we will consider the typical binary gray-code decoding [22] for the phase-unwrapping algorithm; thus, the uncertainty of phase is the uncertainty of the wrapped phase $\sigma_{\phi}^2 = \sigma_{\phi_w}^2$.

Assuming that the demosaicing algorithm's intensity interpolation is accurate, we have three RGB intensities for every pixel. By (15), we can find out how uncertain the phase information from each channel is. Then, we can treat it as a *sensor fusion* problem [31] with three RGB sensors. Although this assumption seems weak, demosaicing accuracy is increased due to developments of gradient-based [35] and AI-based [36] demosaicing algorithms, and we believe using the information from a single wavelength sensor is highly susceptible to the second problem mentioned in Section I, especially when capturing nonuniform color object.

III. PROPOSED METHOD

In this section, we will introduce our method for solving two problems mentioned in Section I. High-level processes of our method, including parameter calibration and 3D reconstruction, are shown in Algorithm 1. The hat notation ($\hat{\cdot}$) denotes LCA-corrected images and pixels. Note that there is no hat for the green channel, which is the reference channel. We would like to emphasize the convenience of our calibration setup, which requires only **two equipments**: checkerboard plate \mathcal{E}_c and white plate \mathcal{E}_w , unlike prior LCA correction algorithms [9], [10], [12].

Algorithm 1 LCAMV

CALIBRATION($\mathcal{E}_c, \mathcal{E}_w$)
 $\mathcal{T} := (\mathbf{K}_c, \mathbf{K}_p, \mathbf{R}, \mathbf{t}) \leftarrow \text{CalibrateStereo}(\mathcal{E}_c)$
 $\boldsymbol{\theta}_c \leftarrow \text{CalibrateCamLCA}(\mathcal{E}_c)$
 $\boldsymbol{\theta}_p \leftarrow \text{CalibratePrjLCA}(\mathcal{E}_w)$
 $\mathbf{k} \leftarrow \text{CalibrateNoise}(\mathcal{E}_w)$
return $\mathcal{T}, \boldsymbol{\theta}_c, \boldsymbol{\theta}_p, \mathbf{k}$

RECONSTRUCTION($\mathbf{I}, \mathcal{T}, \boldsymbol{\theta}_c, \boldsymbol{\theta}_p, \mathbf{k}$)
 $\mathbf{I} := (I_1, I_2, \dots, I_M) \{\text{Captured } M \text{ RGB Images}\}$
 $(\mathbf{I}^R, \mathbf{I}^G, \mathbf{I}^B) \leftarrow \text{ExtractRGB}(\mathbf{I})$
 $(\hat{\mathbf{I}}^R, \hat{\mathbf{I}}^G, \hat{\mathbf{I}}^B) \leftarrow \text{CorrectCamLCA}(\mathbf{I}^R, \mathbf{I}^G, \mathbf{I}^B, \boldsymbol{\theta}_c)$
 $(\phi^R, \phi^G, \phi^B) \leftarrow \text{PhaseAcquisition}(\hat{\mathbf{I}}^R, \hat{\mathbf{I}}^G, \hat{\mathbf{I}}^B)$
 $(u_p^R, u_p^G, u_p^B) \leftarrow \text{ScaleToPixel}(\phi^R, \phi^G, \phi^B)$
 $(\hat{u}_p^R, \hat{u}_p^G, \hat{u}_p^B) \leftarrow \text{CorrectPrjLCA}(u_p^R, u_p^G, u_p^B, \boldsymbol{\theta}_p, \mathcal{T})$
 $\hat{u}_p \leftarrow \text{ChannelFusion}(\hat{u}_p^R, \hat{u}_p^G, \hat{u}_p^B, \hat{\mathbf{I}}^R, \hat{\mathbf{I}}^G, \hat{\mathbf{I}}^B, \mathbf{k})$
 $\hat{z} \leftarrow \text{Triangulate3D}(\mathcal{T}, \hat{u}_p)$
return \hat{z}

A. Lateral Chromatic Aberration Correction

Regarding the LCA effect, the optical properties of the camera and projector are different across the RGB channel. Thus, we have to consider the LCA effect in the camera and projector stereo-vision calibration process. We suggest using a typical black and white checkerboard instead of a red and blue checkerboard [37], which could result in inaccurate phase retrieval as mentioned in the first problem in Section I. For LCA correction, as shown in (11), we must choose the **reference channel** to correct other channels. We decided to use the green channel as a reference channel, which has the highest Bayer filter array density and widest overlapping spectrum in visible light. Then, we can get triangulation parameters \mathcal{T} by stereo-vision calibration using only the green channel. We used local homography refinement [38] for better projector calibration quality, despite using a B/W checkerboard.

We follow prior work's camera LCA calibration and correction [28] method using a B/W checkerboard. Using captured RGB images of a checkerboard, we can extract checkerboard corners from each RGB channel and estimate lateral aberration of each channel with the difference of corner locations. From (11), considering decentering and asymmetry of the image plane, image coordinates are represented as $(x, y) = (au + \dot{u}, v + \dot{v})$. Thus, there are total seven parameters $\boldsymbol{\theta}_c = \{a, \dot{u}, \dot{v}, c_1, c_2, c_3, c_4\}$ for LCA modeling in pixel coordinates. By using the green channel as the reference plane, the total camera LCA parameter consists of $\boldsymbol{\theta}_c = \{\boldsymbol{\theta}_c^R, \boldsymbol{\theta}_c^B\}$ where R, B denote the correcting channel. Refer to [28] for details about the camera LCA model.

1) *Projector LCA Calibration*: After camera LCA calibration and correction, we can now omit the camera LCA and find out the pure effect of projector LCA. Since we cannot directly get projector pixel u_p , we project fringe patterns to a white plate, capture images, conduct phase-shifting (6), phase-unwrapping (7), and scale ϕ to get u_p . Using the camera's RGB channel, we can get projector pixels of different wavelengths (u_p^R, u_p^G, u_p^B) . From now on, we will only notate

the correction of the red channel for simplicity. The lateral difference at the object point viewed at the camera pixel (u_c, v_c) is:

$$\Delta_O^R[u_c, v_c] = u_p^G[u_c, v_c] - u_p^R[u_c, v_c] \quad (18)$$

Recall (12); Δ_O is a linear function of depth, specifically depth from projector z_p . Given u_p^R , we can triangulate to estimate depth $z_p^R = s_p^R$ and the projector's vertical pixel v_p^R using (2) and (3). Then, for every camera pixel (u_c, v_c) that is in the projector's Field of View (FoV), we have $(\Delta_O^R, u_p^R, v_p^R, z_p^R)$. Then, we can remap Δ_O^R and z_p^R into a 2D array in projector pixel (u_p, v_p) , and (12) results in the following:

$$\Delta_O^R[u_p, v_p] = \alpha^R \cdot z_p^R[u_p, v_p] + \beta^R \quad (19)$$

Note that we must use z_p^R calculated from the red channel to correct the red channel independently without using information from other channels. Otherwise, if we use z_p^G or z_p^B , noise at other channels will contribute to the red channel during reconstruction.

Due to the difference between camera and projector resolution, Δ_O^R will contain empty data points, which can be filled by bilinear interpolation like prior works [10], [28].

By gathering multiple observations of $\Delta_O^R[u_p, v_p]$ and $z_p^R[u_p, v_p]$ by varying the white plate's position, we can conduct pixel-wise linear estimation to get 2D arrays of linear coefficients α^R and β^R . Given two linearly correlated random variables $\Delta_O = \alpha \cdot z_p + \beta$, finding the optimal α^* and β^* using the linear minimum mean square error condition [31], [39] is as follows:

$$\alpha^* = \frac{Cov[\Delta_O, z_p]}{Var[z_p]} = \rho_{\Delta_O, z_p} \frac{\sigma_{\Delta_O}}{\sigma_{z_p}} \quad (20a)$$

$$\beta^* = E[\Delta_O] \quad (20b)$$

Using sample mean and sample variance, we can estimate α^R and β^R using data points of Δ_O^R and z_p^R . The blue channel can be corrected in the same manner, resulting in a total of four 2D maps $\theta_p = \{\alpha^R, \beta^R, \alpha^B, \beta^B\}$ for projector LCA correction, as shown in Fig. 6. Note that the unit of α is [pixel/mm], lateral aberration in pixel per depth.

We adjusted white plate locations gradually, increasing z_p from 180 to 340 millimeters far from the projector to cover the camera-projector FoV range, and we used a total of $N = 18$ white plate locations for samples.

2) *Camera Projector LCA correction*: Assuming we now have all parameters $\{\theta_c, \theta_p\}$, we can correct RGB images and projector pixels. For image I^R , we can calculate the corrected pixel and bilinearly interpolate to reconstruct the image without the aberration:

$$(\hat{u}_c^R, \hat{v}_c^R) = (u_c + \Delta_x^R(u_c, v_c, \theta_c^R), v_c + \Delta_y^R(u_c, v_c, \theta_c^R)) \quad (21a)$$

$$\hat{I}^R = \text{Interpolate}(I^R, \hat{u}_c^R, \hat{v}_c^R) \quad (21b)$$

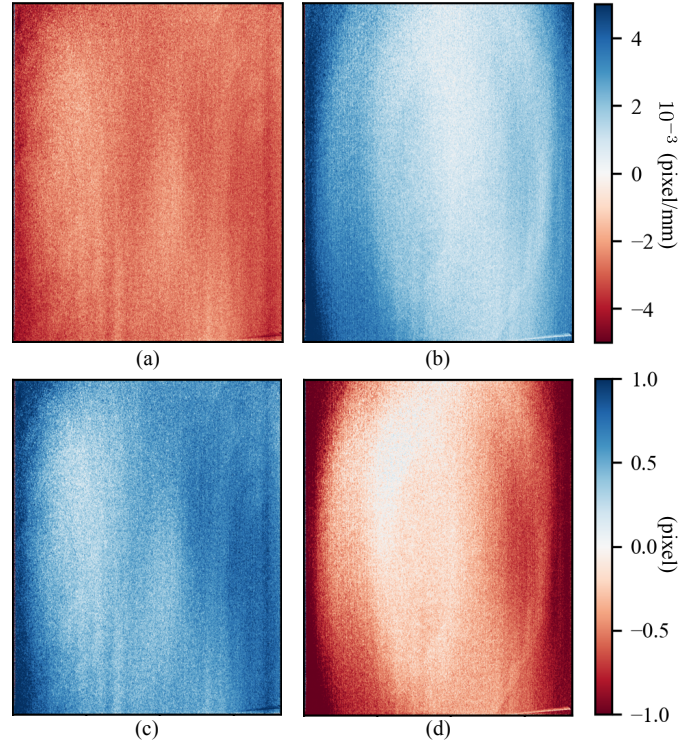


Fig. 6. Projector LCA coefficient map (a) α^R (b) α^B (c) β^R (d) β^B

By camera LCA corrected images \hat{I}^R , we can conduct phase shifting and phase unwrapping to find out projector pixel u_p^R . Then, projector LCA correction is done as follows:

$$(z_p^R, v_p^R) = \text{Triangulate}(u_p^R, \mathcal{T}) \quad (22a)$$

$$\hat{u}_p^R = u_p^R + \Delta_O^R(u_p^R, v_p^R, z_p^R, \alpha^R, \beta^R) \quad (22b)$$

where $\text{Triangulate}(\cdot)$ is done by solving (2) for z_p^R and (3) for v_p^R . For most cases where (u_p, v_p) are not integers, we can bilinear interpolate with the given α and β map. Note that the projector LCA correction of a certain channel is done independently using information from that channel, and the correction is done only for the horizontal pixel, unlike both pixels in the camera LCA correction.

B. Minimum Variance Channel Fusion

Suppose we now have properly aligned projector pixels $(\hat{u}_p^R, u_p^G, \hat{u}_p^B)$ from each channel. We can merge information using the *Minimum Variance Unbiased* (MVU) estimator, where the variance can be calculated as (15). To find out the noise level for each channel, we first have to calibrate for noise coefficients k_0 and k_1 .

1) *Intensity Noise Calibration*: Our intensity noise calibration adopts simple procedures [32] using sample mean and sample variance with varying light conditions. Since we can control the light source by manipulating the projector, we easily apply the prior approach into DFP. Upon projecting P different uniform intensities to the white plate, capture two images for each. For each pair (I_1^u, I_2^u) , the difference between intensity is zero mean $I_1^u - I_2^u = I_\Delta^u \sim \mathcal{N}(0, 2\sigma_n^2)$. We

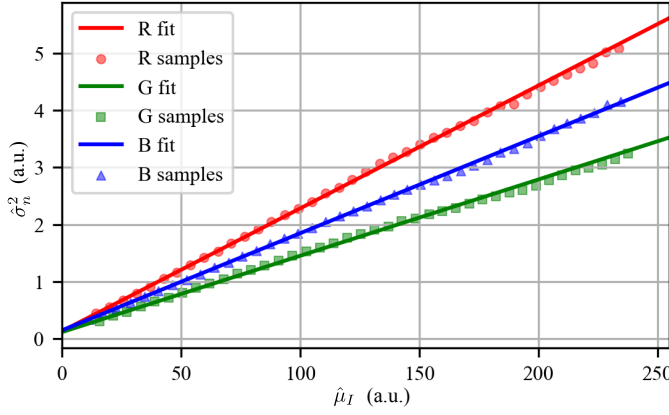


Fig. 7. Calibrated RGB Noise Model Fit

 TABLE I
 CALIBRATED RGB NOISE COEFFICIENT

	Red	Green	Blue
k_0	0.1333	0.1184	0.1500
k_1	0.0215	0.0134	0.0170

use pixel-wise sample mean and sample variance to estimate noiseless intensity μ_I and noise σ_n^2 :

$$\hat{\mu}_I = \frac{1}{2|\mathcal{D}|} \sum_{(u_c, v_c) \in \mathcal{D}} I_1^u[u_c, v_c] + I_2^u[u_c, v_c] \quad (23a)$$

$$\hat{\mu}_\Delta = \frac{1}{|\mathcal{D}|} \sum_{(u_c, v_c) \in \mathcal{D}} I_1^u[u_c, v_c] - I_2^u[u_c, v_c] \quad (23b)$$

$$\hat{\sigma}_n^2 = \frac{1}{2(|\mathcal{D}| - 1)} \sum_{(u_c, v_c) \in \mathcal{D}} (I_\Delta^u[u_c, v_c] - \hat{\mu}_\Delta)^2 \quad (23c)$$

where \mathcal{D} denotes the pixel domain where nearly the same level of light is projected, $\hat{\mu}_\Delta$ is the domain sample mean of I_Δ , and $\hat{\sigma}_n$ is the estimated sample variance. Given P data points of $(\hat{\mu}_I, \hat{\sigma}_n^2)$ pairs, we can conduct weighted line fitting, which is a maximum likelihood estimate for (k_0, k_1) :

$$\chi^2 = \sum_{i=1}^P \frac{(\hat{\sigma}_{n_i}^2 - (k_0 + k_1 \cdot \hat{\mu}_{I_i}))^2}{Var[\hat{\sigma}_{n_i}^2]} \quad (24)$$

where $Var[\hat{\sigma}_n^2]$ can be approximated under the Gaussian assumption:

$$Var[\hat{\sigma}_n^2] \approx \frac{2(\hat{\sigma}_n^2)^2}{(|\mathcal{D}| - 1)} \quad (25)$$

We can estimate noise parameters (k_0, k_1) by minimizing (24). Refer to [32] for details about the noise calibration model. By calibrating for all channels, we have total six parameters. $\mathbf{k} = \{k_0^R, k_1^R, k_0^G, k_1^G, k_0^B, k_1^B\}$. Fig. 7 and Table. I is the calibrated result for the Poisson-Gaussian noise model, using $P = 40$ different intensity levels with $|\mathcal{D}| \approx 140000$ pixels. It can be found out that the red channel is the noisiest channel and the green channel is the least.

2) *RGB Channel Fusion*: Given noise parameters \mathbf{k} , we can find out the variance of the phase from each channel using

(16). We use the weighted average to estimate the optimal \hat{u}_p , where the following should hold:

$$\hat{u}_p = w_R \hat{u}_p^R + w_G u_p^G + w_B \hat{u}_p^B \quad (26a)$$

$$1 = w_R + w_G + w_B \quad (26b)$$

$$\mathbf{w} = \arg \min_{\mathbf{w}} (Var[\hat{u}_p]) \quad (26c)$$

where $\mathbf{w} = [w_R, w_G, w_B]$ is the weight vector, (26b) denotes the unbiased condition and (26c) denotes the minimum variance condition. Using the Poisson-Gaussian assumption, where each channel is statistically independent, variance leads to:

$$Var[\hat{u}_p] = w_R^2 Var[\hat{u}_p^R] + w_G^2 Var[u_p^G] + w_B^2 Var[\hat{u}_p^B] \quad (27)$$

The variance of the projector pixel is simply a scaled version of the variance of the phase. Neglecting the uncertainty induced by the LCA correction, we can calculate the uncertainty of the projector pixel as

$$Var[\hat{u}_p] = w_R^2 \sigma_{u_p^R}^2 + w_G^2 \sigma_{u_p^G}^2 + w_B^2 \sigma_{u_p^B}^2 \quad (28a)$$

$$\sigma_{u_p^i}^2 = (\lambda/2\pi)^2 \cdot \sigma_{\phi^i}^2, \quad i \in \{R, G, B\} \quad (28b)$$

where $(\lambda/2\pi)$ is the coefficient scaling phase to projector pixel, and $\sigma_{\phi^i}^2$ is the uncertainty of phase from each channel calculated by (16). The solution for minimizing (28) with constraints can be done using the Cauchy-Schwartz inequality. Let two vectors be $\mathbf{a}_1 = [w_R \sigma_{u_p^R}, w_G \sigma_{u_p^G}, w_B \sigma_{u_p^B}]$, $\mathbf{a}_2 = [1/\sigma_{u_p^R}, 1/\sigma_{u_p^G}, 1/\sigma_{u_p^B}]$. Dividing $\|\mathbf{a}_2\|^2$ to the each side of $|\langle \mathbf{a}_1, \mathbf{a}_2 \rangle|^2 \leq \|\mathbf{a}_1\|^2 \|\mathbf{a}_2\|^2$ leads to:

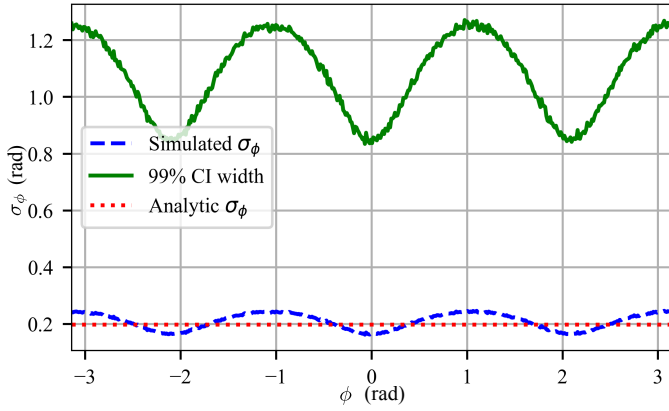
$$\frac{(w_R + w_G + w_B)^2}{\|\mathbf{a}_2\|^2} = \frac{1}{\|\mathbf{a}_2\|^2} \leq (w_R^2 \sigma_{u_p^R}^2 + w_G^2 \sigma_{u_p^G}^2 + w_B^2 \sigma_{u_p^B}^2) \quad (29)$$

Then the right side $Var[\hat{u}_p]$ is lower bounded, and the equality holds when \mathbf{a}_1 and \mathbf{a}_2 are the scalar multiple of each other. Under this condition, solving for optimal \mathbf{w}^* leads to:

$$w_i^* = \frac{1/\sigma_{u_p^i}^2}{\sum_j 1/\sigma_{u_p^j}^2}, \quad i, j \in \{R, G, B\} \quad (30)$$

Note that optimal scalar weights \mathbf{w}^* can be calculated deterministically after finding uncertainties. Since w_R, w_G, w_B are never 0 unless $\sigma_{u_p^i}^2$ goes to infinity, this method is still susceptible to the outlier information from noisy channels. Since the phase unwrapping algorithm incorporates discontinuities, the outlier channel can have catastrophic 2π jump errors. To remove the effect of the outlier channel, we exploit the fact that we know the variance $\sigma_{u_p^i}^2$ of the projector pixel, although its distribution is unknown and non-Gaussian.

We use the *Monte Carlo method* [40] to approximate the Confidence Interval (CI) of the unknown ϕ distribution. Note that u_p is simply the scalar multiple of ϕ ; thus, the CI of u_p is also the scaled version of ϕ . For the Monte Carlo method, we used a total of $N = 10000$ samples with the feasible intensity noise level $k_0 = 0.0133, k_1 = 0.1212$ from the noise calibration of the Poisson-Gaussian model (14), and the feasible ratio between mean and modulation intensities


 Fig. 8. Standard deviation and confidence interval of ϕ

($I_A : I_B = 2 : 1$). We simulated three intensities using (5) and forwarded them to the three-step phase shifting algorithm (6) to approximate the unknown distribution of ϕ , ranging in $[-\pi, +\pi)$. Note that the phase-shifting algorithm returns wrapped phase; thus, circular mean and circular standard deviation [41] were used to calculate statistics:

$$\bar{R} = \frac{1}{N} \sum_{i=1}^N \exp(j\phi_i), \quad (31a)$$

$$\mu_{\phi_{2\pi}} = \arg(\bar{R}), \quad (31b)$$

$$\sigma_{\phi_{2\pi}} = \sqrt{-2 \ln |\bar{R}|} \quad (31c)$$

where $\mu_{\phi_{2\pi}}$ is the circular mean, $\sigma_{\phi_{2\pi}}$ is the circular standard deviation, and j is the imaginary unit. As shown in Fig. 8, it could be found that the simulated sample standard deviation oscillates around the analytically calculated σ_{ϕ} using (16) in the phase domain. The mean 99% CI across the phase domain was found to be $\pm 2.72\sigma_{\phi}$.

To filter out the outlier channel, we define the least uncertain channel as the anchor channel and find if the u_p from other channels are in the anchor channel's 99% CI. If the projector pixel from a certain channel is not in the CI, we mask that channel's uncertainty to infinity and reassign the weights using (30). The outlier channel filtering process can be mathematically expressed as:

$$\sigma_{u_p^i}^{\prime 2} = \begin{cases} \infty, & \text{if } |u_p^i - u_p^\dagger| > 2.72 \sigma_{u_p^\dagger} \\ \sigma_{u_p^i}^2, & \text{otherwise} \end{cases} \quad (32a)$$

$$\dagger := \arg \min_i (\sigma_{u_p^i}^2), \quad i \in \{R, G, B\} \quad (32b)$$

where \dagger is the anchor channel and $\sigma_{u_p^i}^{\prime 2}$ is the refined uncertainties to re-assign the weights, neglecting the outlier channel. Note that the hat notation is skipped, but u_p^i, u_p^\dagger denotes the LCA-corrected projector pixel if the channel is red or blue. Then, the reassigned weights will omit the effect of the outlier channel. Given new weights, the optimal \hat{u}_p can be calculated, and the 3D geometry \hat{z} can be acquired by triangulation (2).

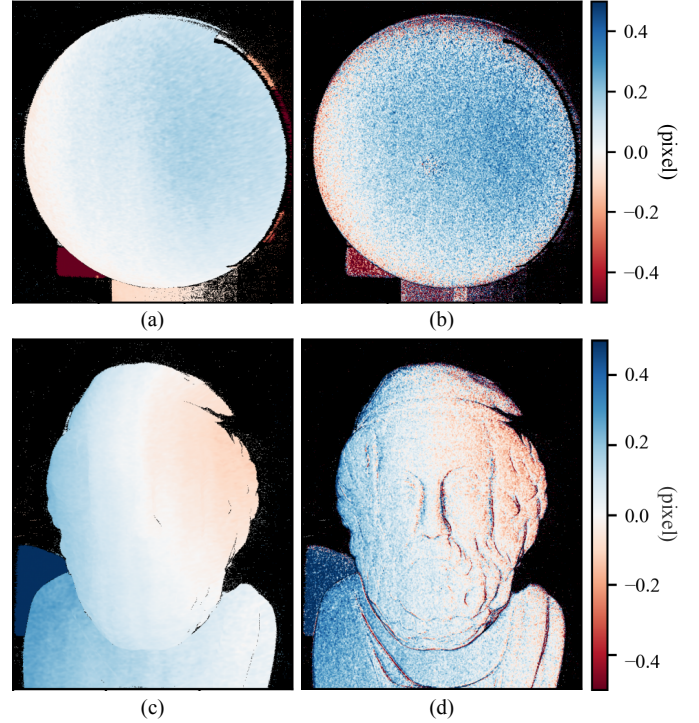

 Fig. 9. $\hat{\Delta}_O, \Delta_O$ while scanning white sphere and sculpture (a) $\hat{\Delta}_O^R$ (b) Δ_O^R (c) $\hat{\Delta}_O^B$ (d) Δ_O^B


Fig. 10. Image of White Sphere and Sculpture

IV. EXPERIMENTAL RESULT

In this section, we will show the validity of LCAMV by real-world experiments. In Section IV-A, we will show experimental results explaining one of our main contributions: the projector LCA model and correction. Then, we will show increased 3D geometry precision of LCAMV compared to typical RGB to grayscale intensity baselines. In Section IV-B, we will show the LCA correction stage and the minimum variance channel fusion stage effect on precise 3D reconstruction of colored objects by ablation study. Lastly, we will compare the quality of 3D geometry of nonuniform color objects with complex geometry using the proposed method with other baselines. All of our experiments were conducted with the Grasshopper3 GS3-U3-23S6C-C and TI DLP LightCrafter 4500 for hardware setups.

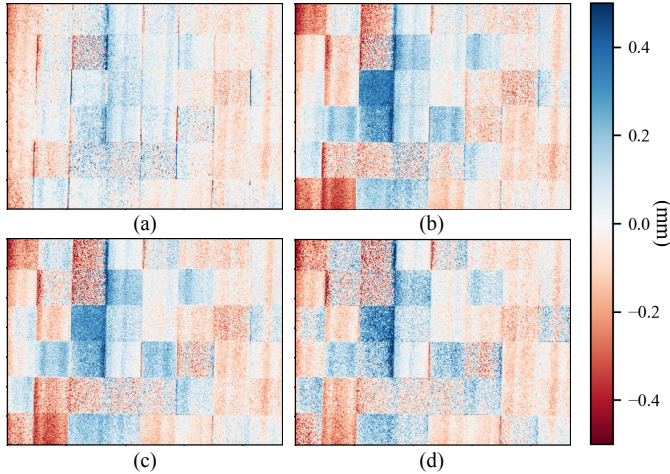


Fig. 11. Colorboard plane fitting error map using (a) LCAMV (b) Mean (c) Y'UV (d) Green

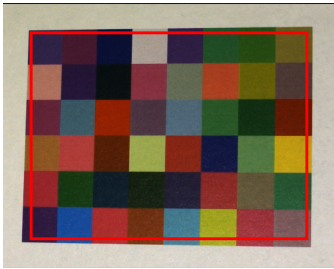


Fig. 12. ROI and image of Colorboard

A. Quantitative Analysis

1) *LCA Model Analysis*: We have weakly proven the validity of our theoretical model for LCA at the object Δ_O with scanning white plates and using the Pearson correlation coefficient in Section II. However, can this model be applied to general non-planar objects? If our theoretical model is truly valid, the estimated $\hat{\Delta}_O$ and the observed Δ_O should show the similar trend on objects of any geometry. To find out, we calculated the observed lateral aberration $\Delta_O^R[u_c, v_c] = u_p^G[u_c, v_c] - u_p^R[u_c, v_c]$, while scanning the white non-planar objects. We compare $\hat{\Delta}_O$ and Δ_O by scanning the white, complex objects as shown in Fig. 9. Two objects are shown in Fig. 10. The top two figures are Δ_O^B and $\hat{\Delta}_O^B$ while scanning the white sphere, and the two figures at the bottom are Δ_O^R and $\hat{\Delta}_O^R$ while scanning the white sculpture. It can be found out that the projector LCA of the red channel is about +0.3 pixel, and the blue channel varies around -0.25 pixel to +0.25 pixel on each object. Comparing the actual and the estimated projector LCA, Δ_O looks like a noisy version of $\hat{\Delta}_O$ due to stochasticity, but the overall heatmap across local regions looks similar.

2) *Colorboard Plane Fitting*: To prove the improved precision of LCAMV in scanning nonuniform color objects, we have created a colorboard with checker patterns of a total of 6×8 random colors. Then, we have printed out the colorful checker pattern and attached it to the flat plate, as flat as possible. To show the LCAMV's superiority across all general

TABLE II
COLORBOARD PLANE FITTING MSE

Method	MSE (mm ²)			
	LCAMV	Mean	Y'UV	Green
3-Step	0.036073	0.055645	0.064706	0.082067
12-Step	0.014794	0.027995	0.029057	0.038311
18-Step	0.012485	0.024468	0.024343	0.032854

phase-shifting algorithms, we scanned a colorboard using 3, 12, and 18-step phase-shifted patterns with a wavelength of $\lambda = 36$ pixels and a phase period of $L = 32$ using binary graycode decoding for the phase unwrapping algorithm, with an exposure time of 7 milliseconds. To minimize the camera and projector distortion effect on plane fitting error, we placed the colorboard plate far enough away, about $z \approx 320$ millimeters away from the camera. From the acquired depth image, we manually masked the Region of Interest (ROI) of the colorboard as shown in Fig. 12. Since the number of point clouds in ROI is too large ($N \approx 160000$) for the plane fitting algorithm, we randomly subsampled 10,000 points in ROI to define the plane and used all points to calculate the plane fitting error. We compared LCAMV with other baselines using mean intensity, Y'UV transform, and only the green channel.

For all baselines, we could find out that an increased number of patterns leads to better precision, which is theoretically correct. Most importantly, we could find out that LCAMV's plane fitting error is consistently lower than any other baseline. Compared to the second-best baselines, LCAMV shows **43.6%** reduced plane fitting error on average, which shows the robust performance of LCAMV. Fig. 11 is a comparison of the error map of each baseline where 18 steps were used. It can be found out that Mean, Y'UV, and Green exhibit error regions clearly divided into blocks of yellow, cyan, red, and blue colors, which is due to the LCA effect induced by different colors of checker blocks. While LCAMV's error is similar locally across checker blocks, despite the small portion of yellow and cyan regions due to camera and projector distortion. For all baselines, it could be seen that high error is present at the vertical block boundaries, which are known as Discontinuity-induced Measurement Artifacts (DMA) [42]–[44]. DMA is induced by the blur at the abrupt change in irradiation level, rather than irradiation wavelength. Since DMA is unrelated to the LCA effect, we will treat DMA correction as out of this paper's scope. The green channel's performance was the worst, due to the absence of the averaging effect of noise, unlike Mean and Y'UV. Surprisingly, using only the green channel could not solve the LCA problem perfectly, as shown in Fig. 11. This is because both the projector's and the camera's channels treat color as wavelengths of a continuous spectrum, not a single wavelength. Since the projector and the camera do not project and scan exactly one single wavelength, overlapping spectra of red and blue lights still affect the information in the green channel. Inferred from this result, using a monochrome camera can also suffer from LCA when scanning nonuniform colored objects; thus, LCAMV is the only promising solution when scanning nonuniform color objects. We will also qualitatively show that using the green channel cannot fully solve the LCA

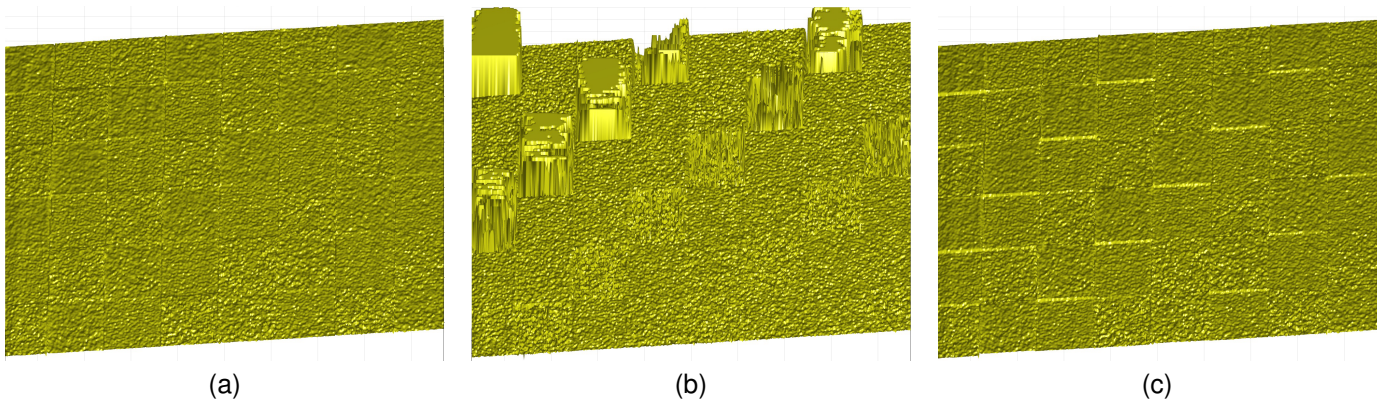


Fig. 13. RGB board rendering comparison using (a) LCAMV (b) LCA (c) MV

effect in Section IV-C.

B. Ablation Study

Next, for further understanding of LCAMV’s stages, we conduct the ablation study with two modified methods: LCA and MV. LCA only conducts LCA correction, but the resulting projector pixel is the mean of LCA corrected projector pixels from each channel. MV does not conduct any LCA corrections, but projector pixels from each channel are merged with the MVU manner. To clearly visualize the difference and observe each stage’s contribution, we created an RGB board, similar to the prior experiment. We compare three methods with plane fitting error and rendered visualization of 18-step reconstruction. Experiment setups are the same as with the prior colorboard plane fitting experiment, and the image of the RGB board and ROI is shown in Fig. 14.

Plane fitting mean squared error was the lowest at LCAMV for all methods. Note that the LCA method failed and showed extremely high plane fitting error due to the absence of weight filtering described in (32). Fig. 13 is the reconstructed rendering of the RGB board reconstructed using the 18-step phase-shifting algorithm. It can be found out that block artifacts are visible in MV unlike LCAMV. Although LCA fixes the block artifacts by LCA correction, the reconstructed surface looks comparatively rough due to high noise, and the blocks of red color at the top left region are corrupted by the outlier blue channel’s catastrophic 2π jump error. On the other hand, the incorporated method LCAMV corrects LCA effectively, exhibits less noise using the MVU condition, and omits the effect of the outlier channel. The ablation study shows that both the LCA correction stage and the minimum variance fusion stage work complementarily to achieve the best performance.

C. Qualitative Analysis

Lastly, to extensively validate LCAMV’s performance on general non-planar nonuniform color objects, we printed out RGB stripe patterned paper and arbitrarily created a curvy surface and a zigzagged surface as shown in Fig. 17. We compare the ROI region’s rendered result with the second-best baseline from colorboard plane fitting: mean intensity

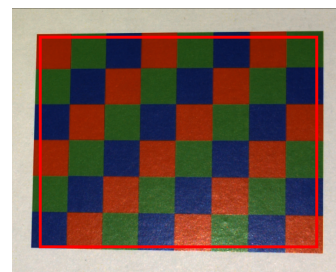


Fig. 14. ROI and image of colorboard

TABLE III
RGB BOARD PLANE FITTING MSE

Method	MSE (mm ²)		
	LCAMV	LCA (Abl.)	MV (Abl.)
3-Step	0.030582	282.76	0.066288
12-Step	0.016121	295.12	0.054010
18-Step	0.014217	299.32	0.052371

and the green channel to test if the pseudo-monochrome camera can solve the LCA effect. We used the 18-step phase-shifting algorithm and 6 milliseconds for the exposure time for qualitative analysis. The remaining experiment setups are the same as the colorboard plane fitting experiment.

As shown in Fig. 15 and Fig. 16, it is clearly visible that rendered rows of different colors show different surface levels for the mean and green baselines due to the LCA effect. Unlike Mean and Green, the rendered result of LCAMV does not show any bumpy artifacts, and it is hard to tell where the color stripes’ boundaries are located. Surprisingly, using the pseudo-monochrome information from the green channel showed less bumpy artifacts than the mean intensity, but it could not fully solve the LCA effect. Again, this result shows that LCAMV with the RGB camera is the only solution to solve the LCA effect while scanning nonuniform color objects.

V. CONCLUSION

This paper proposes LCAMV, the algorithm that can robustly reconstruct 3D geometry of nonuniform color objects. LCAMV consists of two stages: LCA correction and minimum variance channel fusion. The LCA correction stage effectively

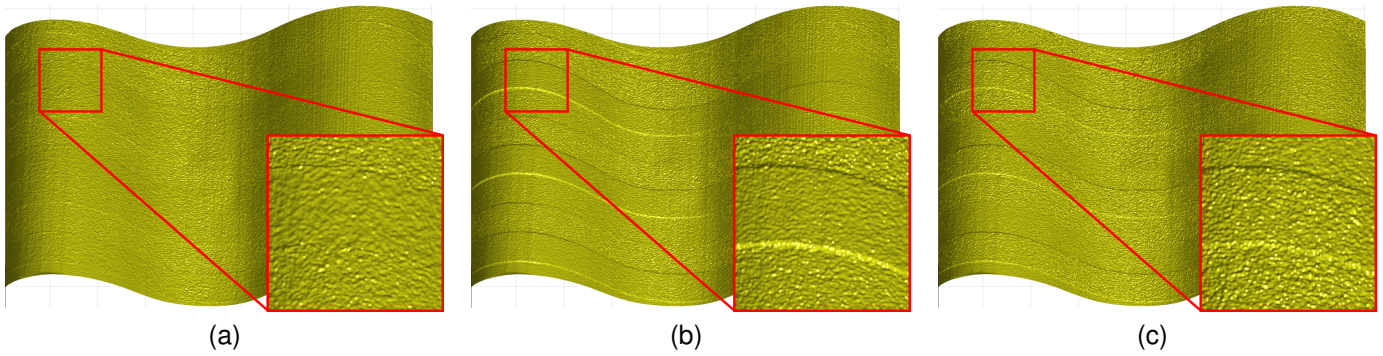


Fig. 15. Curvy RGB surface rendering comparison using (a) LCAMV (b) Mean (c) Green

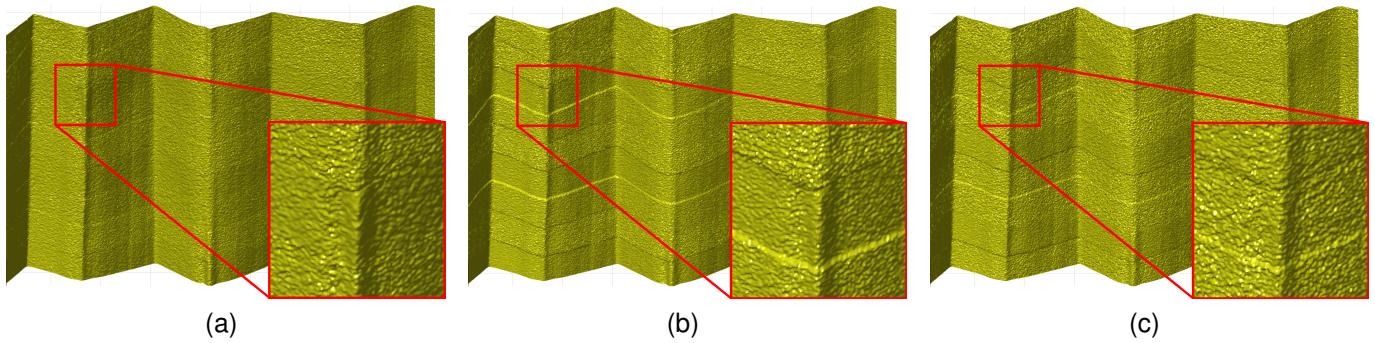


Fig. 16. Zigzagged RGB surface rendering comparison using (a) LCAMV (b) Mean (c) Green

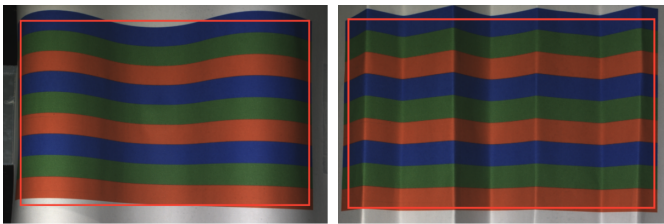


Fig. 17. ROI and image of RGB surface (a) curvy (b) zigzagged

compensates for the bias of each channel, especially that induced by the projector’s LCA. The minimum variance channel fusion stage merges the information from each channel with the highest precision. We believe that LCAMV is the solution bridging DFP in controlled laboratory conditions to more practical and industrial conditions, where the objects could be in any color, and accurate RGB-D data is required.

However, the complexity of the algorithm is a limitation for future improvements. Although every part of the LCAMV algorithm is deterministic and does not include any iterative optimizations, the computation burden is obviously larger than the typical phase-shifting and triangulation algorithm. Optimization of the LCAMV algorithm might be required for the real-time RGB-D acquisition.

ACKNOWLEDGEMENT

This research was supported by the Technology Innovation Program(Project Name: Development of AI autonomous continuous production system technology for gas turbine blade

maintenance and regeneration for power generation, Project Number: RS-2025-25447257, Contribution Rate: 50%) funded By the Ministry of Trade, Industry and Resources(MOTIR, Korea), the Culture, Sports and Tourism R&D Program through the Korea Creative Content Agency grant funded by the Ministry of Culture, Sports and Tourism in 2024 (Project Name: Global Talent for Generative AI Copyright Infringement and Copyright Theft, Project Number: RS-2024-00398413, Contribution Rate: 40%), and the National Research Foundation of Korea(NRF) grant funded by the Korea government(MSIT) (Project Number: RS-2025-16072782, Contribution Rate: 10%).

REFERENCES

- [1] R. Wang, A. C. Law, D. Garcia, S. Yang, and Z. Kong, “Development of structured light 3d-scanner with high spatial resolution and its applications for additive manufacturing quality assurance,” *The International Journal of Advanced Manufacturing Technology*, vol. 117, no. 3, pp. 845–862, 2021.
- [2] O. V. Olesen, R. R. Paulsen, L. Hojgaard, B. Roed, and R. Larsen, “Motion tracking for medical imaging: a nonvisible structured light tracking approach,” *IEEE transactions on medical imaging*, vol. 31, no. 1, pp. 79–87, 2011.
- [3] L. Yang, Y. Liu, and J. Peng, “Advances techniques of the structured light sensing in intelligent welding robots: a review,” *The International Journal of Advanced Manufacturing Technology*, vol. 110, no. 3, pp. 1027–1046, 2020.
- [4] C. Anthes, R. J. García-Hernández, M. Wiedemann, and D. Kranzlmüller, “State of the art of virtual reality technology,” in *2016 IEEE aerospace conference*. IEEE, 2016, pp. 1–19.
- [5] T. Zhang, Z. McCarthy, O. Jow, D. Lee, X. Chen, K. Goldberg, and P. Abbeel, “Deep imitation learning for complex manipulation tasks from virtual reality teleoperation,” in *2018 IEEE international conference on robotics and automation (ICRA)*. Ieee, 2018, pp. 5628–5635.

- [6] B. Mildenhall, P. P. Srinivasan, M. Tancik, J. T. Barron, R. Ramamoorthi, and R. Ng, "Nerf: Representing scenes as neural radiance fields for view synthesis," *Communications of the ACM*, vol. 65, no. 1, pp. 99–106, 2021.
- [7] B. Kerbl, G. Kopanas, T. Leimkühler, and G. Drettakis, "3d gaussian splatting for real-time radiance field rendering," 2023. [Online]. Available: <https://arxiv.org/abs/2308.04079>
- [8] A. Goyal, J. Xu, Y. Guo, V. Blukis, Y.-W. Chao, and D. Fox, "Rvt: Robotic view transformer for 3d object manipulation," in *Conference on Robot Learning*. PMLR, 2023, pp. 694–710.
- [9] C. Chen and B. Pan, "Correcting lateral chromatic aberration using orthogonal fringe patterns," *Applied Optics*, vol. 59, no. 22, pp. 6517–6525, 2020.
- [10] J. Huang, Q. Xue, Z. Wang, and J. Gao, "Analysis and compensation for lateral chromatic aberration in a color coding structured light 3d measurement system," *Sensors*, vol. 16, no. 9, p. 1426, 2016.
- [11] C. Chen, Z. Zhang, F. Gao, and H. Wang, "A flexible lateral chromatic aberration correction method for a color-encoded fringe projection system," *Optics and Lasers in Engineering*, vol. 162, p. 107425, 2023.
- [12] P.-P. Sun, Q. Xue, W. Ji, H. Meng, X. Sun, and X. Yang, "Analysis and compensation of lateral chromatic aberration of structured light 3d measurement system," *Optics Communications*, vol. 488, p. 126871, 2021.
- [13] D. L. MacAdam, "Projective transformations of ici color specifications," *JOSA*, vol. 27, no. 8, pp. 294–299, 1937.
- [14] S. Zhang and P. Huang, "High-resolution, real-time 3d shape acquisition," in *2004 Conference on Computer Vision and Pattern Recognition Workshop*. IEEE, 2004, pp. 28–28.
- [15] S. Zhang and S.-T. Yau, "Simultaneous three-dimensional geometry and color texture acquisition using a single color camera," *Optical Engineering*, vol. 47, no. 12, pp. 123 604–123 604, 2008.
- [16] P. Ou, B. Li, Y. Wang, and S. Zhang, "Flexible real-time natural 2d color and 3d shape measurement," *Optics express*, vol. 21, no. 14, pp. 16 736–16 741, 2013.
- [17] Y. Xu, C. Chen, S. Huang, and Z. Zhang, "Simultaneously measuring 3d shape and colour texture of moving objects using ir and colour fringe projection techniques," *Optics and Lasers in Engineering*, vol. 61, pp. 1–7, 2014.
- [18] J. Wang, Y. Zhou, and Y. Yang, "Rapid 3d measurement technique for colorful objects employing rgb color light projection," *Applied Optics*, vol. 59, no. 7, pp. 1907–1915, 2020.
- [19] H. Yuan, H. Li, G. Feng, Z. Bao, W. Li, and L. Cui, "Absolute phase retrieval for colored objects based on three phase-shifting amount codes," *Optics Express*, vol. 28, no. 26, pp. 38 491–38 504, 2020.
- [20] Y. Ma, S. Soatto, J. Košecák, and S. Sastry, *An invitation to 3-d vision: from images to geometric models*. Springer, 2004, vol. 26.
- [21] K. Creath, "V phase-measurement interferometry techniques," in *Progress in optics*. Elsevier, 1988, vol. 26, pp. 349–393.
- [22] G. Sansoni, M. Carocci, and R. Rodella, "Three-dimensional vision based on a combination of gray-code and phase-shift light projection: analysis and compensation of the systematic errors," *Applied optics*, vol. 38, no. 31, pp. 6565–6573, 1999.
- [23] S. Zhang, "Absolute phase retrieval methods for digital fringe projection profilometry: A review," *Optics and lasers in engineering*, vol. 107, pp. 28–37, 2018.
- [24] C. Zuo, L. Huang, M. Zhang, Q. Chen, and A. Asundi, "Temporal phase unwrapping algorithms for fringe projection profilometry: A comparative review," *Optics and lasers in engineering*, vol. 85, pp. 84–103, 2016.
- [25] J. H. Bruning, D. R. Herriott, J. E. Gallagher, D. P. Rosenfeld, A. D. White, and D. J. Brangaccio, "Digital wavefront measuring interferometer for testing optical surfaces and lenses," *Applied optics*, vol. 13, no. 11, pp. 2693–2703, 1974.
- [26] J. E. Greivenkamp, "Generalized data reduction for heterodyne interferometry," *Optical Engineering*, vol. 23, no. 4, pp. 350–352, 1984.
- [27] M. Born and E. Wolf, *Principles of optics: electromagnetic theory of propagation, interference and diffraction of light*. Elsevier, 2013.
- [28] J. Mallon and P. F. Whelan, "Calibration and removal of lateral chromatic aberration in images," *Pattern recognition letters*, vol. 28, no. 1, pp. 125–135, 2007.
- [29] R. J. Carroll, D. Ruppert, L. A. Stefanski, and C. M. Crainiceanu, *Measurement error in nonlinear models: a modern perspective*. Chapman and Hall/CRC, 2006.
- [30] "Ti dlp® system design: Optical module specifications," Texas Instruments, Application Report DLPA078C, October 2024, rev. C, originally published February 2017. [Online]. Available: <https://www.ti.com/lit/pdf/DLPA078>
- [31] A. Leon-Garcia, *Probability, statistics, and random processes for electrical engineering*. Pearson Education, 2017.
- [32] G. E. Healey and R. Kondepudy, "Radiometric ccd camera calibration and noise estimation," *IEEE Transactions on pattern analysis and machine intelligence*, vol. 16, no. 3, pp. 267–276, 2002.
- [33] A. Foi, M. Trimeche, V. Katkovnik, and K. Egiazarian, "Practical poissonian-gaussian noise modeling and fitting for single-image raw-data," *IEEE transactions on image processing*, vol. 17, no. 10, pp. 1737–1754, 2008.
- [34] J. Wang and Y. Yang, "Phase extraction accuracy comparison based on multi-frequency phase-shifting method in fringe projection profilometry," *Measurement*, vol. 199, p. 111525, 2022.
- [35] X. Li, B. Gunturk, and L. Zhang, "Image demosaicing: A systematic survey," in *Visual Communications and Image Processing 2008*, vol. 6822. SPIE, 2008, pp. 489–503.
- [36] M. Gharbi, G. Chaurasia, S. Paris, and F. Durand, "Deep joint demosaicking and denoising," *ACM Transactions on Graphics (ToG)*, vol. 35, no. 6, pp. 1–12, 2016.
- [37] S. Zhang and P. S. Huang, "Novel method for structured light system calibration," *Optical Engineering*, vol. 45, no. 8, pp. 083 601–083 601, 2006.
- [38] D. Moreno and G. Taubin, "Simple, accurate, and robust projector-camera calibration," in *2012 Second International Conference on 3D Imaging, Modeling, Processing, Visualization & Transmission*. IEEE, 2012, pp. 464–471.
- [39] S. M. Kay, *Fundamentals of statistical signal processing: estimation theory*. Prentice-Hall, Inc., 1993.
- [40] N. Metropolis and S. Ulam, "The monte carlo method," *Journal of the American statistical association*, vol. 44, no. 247, pp. 335–341, 1949.
- [41] K. V. Mardia and P. E. Jupp, *Directional statistics*. John Wiley & Sons, 2009.
- [42] H. Yue, H. G. Dantanarayana, Y. Wu, and J. M. Huntley, "Reduction of systematic errors in structured light metrology at discontinuities in surface reflectivity," *Optics and Lasers in Engineering*, vol. 112, pp. 68–76, 2019.
- [43] C. Blanchard and S. Zhang, "Removal of phase artifacts from high-contrast texture for 3d fringe projection system," in *Dimensional Optical Metrology and Inspection for Practical Applications XI*, vol. 12098. SPIE, 2022, pp. 19–30.
- [44] S. Chen, R. Xia, J. Zhao, H. Zhang, and M. Hu, "Analysis and reduction of phase errors caused by nonuniform surface reflectivity in a phase-shifting measurement system," *Optical Engineering*, vol. 56, no. 3, pp. 033 102–033 102, 2017.